J. Fluid Mech. (1988), *vol.* 191, *pp.* 47–77
Printed in Great Britain

Separation of three-dimensional laminar boundary layers on a prolate spheroid

By TUNCER CEBECI AND WENHAN SU†
Aerodynamics Research and Technology, Douglas Aircraft Company, Long Beach, CA 90846, USA

(Received 25 February 1987)

The laminar flow around a prolate spheroid at 6° angle of attack has been determined by the numerical solution of steady, three-dimensional boundary-layer equations with the external-pressure distribution obtained from an analytic solution of the inviscid-flow equations. The flow is shown to comprise a region of positive crossflow, followed by a substantial region of negative crossflow, a separation line and two terminal lines beyond which solutions of the boundary-layer equations could not be obtained. The separation line defines one boundary of a region of open separation and accords with the argument of Lighthill in that separation of three-dimensional boundary-layer flows is defined by a skin-friction line. A procedure is described that permits the identification of this skin-friction line and requires that it passes through the first location at which the longitudinal component of the wall shear is zero and the circumferential component negative. The numerical tests show that the finite-difference scheme based on the characteristic box allows calculations against the circumferential flow and with an accuracy equal to that of the regular box provided that a stability criterion is used to choose the grid intervals. This stability criterion is shown to be essential for accurate solutions in the vicinity of the separation and terminal lines and implies the need for extremely fine grids. It is evident that similar numerical constraints will apply to calculations performed with an interactive boundary-layer procedure or with higher-order forms of the Navier–Stokes equations.

1. Introduction

Considerable attention has been paid in the last two decades to the subject of three-dimensional boundary layers, and much of this has considered the problem of solving three-dimensional boundary layers with the external boundary condition provided in the form of a pressure distribution. As is shown by Cebeci (1986*a*) the boundary-layer equations can be solved accurately for a range of pressure distributions, provided that these do not give rise to strong negative crossflows. Unfortunately, strong negative cross flows exist in practice and an appropriate procedure for their representation is required.

The principle of the existence of zones of influence and dependence for boundary-layer flows was postulated by Raetz (1957) and, in large measure explains the difficulty posed by negative crossflow velocities. The boundary-layer equations are diffusive in the direction normal to the body and wave-like in planes parallel to the surface so that the direction of propagation must be recognized as being along the local stream direction. Since this direction varies across the boundary layer, it is

---

† Center for Aerodynamics Research, California State University, Long Beach, CA, USA.

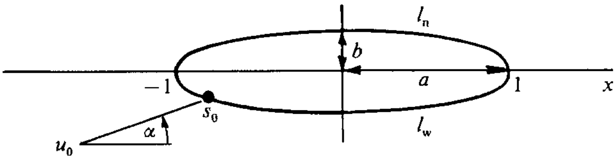

FIGURE 1. Notation for prolate spheroid at incidence α: l_w and l_n denote windward and leeward sides with s_0 representing the stagnation point.

possible to identify zones of influence and dependence for any point. In calculation terms, this implies that a marching procedure may have to identify the correct direction in which to march if the need for downstream boundary conditions is to be avoided and the requirements of the zones of influence and dependence met. This need was recognized, but not entirely fulfilled, by Cebeci, Khattab & Stewartson (1981) with their development and application of the characteristic-box numerical scheme.

A related problem of three-dimensional flows is the nature of separation and the precision of means to deal with it in a numerical procedure for the solution of boundary-layer equations. Maskell (1955) and Lighthill (1963) expressed different views and many authors have sought resolution of the consequent uncertainty though, in retrospect, it appears that none of the methods has been able to overcome inherent numerical difficulties.

The problems of the previous two paragraphs are resolved by the present calculations which solve the three-dimensional boundary-layer equations with the characteristic-box scheme. This scheme ensures that the numerical grid satisfies a criterion for numerical stability and, as a consequence, that the solutions are accurate.

To address the problem of solving three-dimensional boundary-layer equations and study the nature of flow separation in three-dimensional flows, we consider laminar flow over a prolate spheroid in the coordinate system of figure 1. The equation of a prolate spheroid can be written as

$$\left(\frac{x}{a}\right)^2+\left(\frac{r_0}{b}\right)^2=1 \tag{1}$$

and the geometric parameters and the inviscid velocity distribution can be obtained from analytical expressions as we shall describe in §2.

If we denote the circumferential, longitudinal and normal directions by θ, x and y, respectively, then the solution of the three-dimensional boundary-layer equations requires initial conditions along the intersecting (x,y)- and (θ,y)-planes. Those on the (x,y)-plane can be obtained from equations that take into account the symmetry of the flow and those on the (θ,y)-plane depend on the coordinate system and require special procedures as described, for example, in Cebeci, Kaups & Khattab (1986). With a body-oriented coordinate system, the geometric parameters have a singularity at the nose and this can be removed by suitable transformations so that the boundary-layer equations can be solved to generate initial conditions in the (x,y)- and (θ,y)-planes as discussed by Cebeci, Khattab & Stewartson (1980).

The flow on a body of revolution at incidence usually has one plane of symmetry but two initial (x,y)-planes, one on the windward side and the other on the leeward side. The solution of the full three-dimensional boundary-layer equations can be

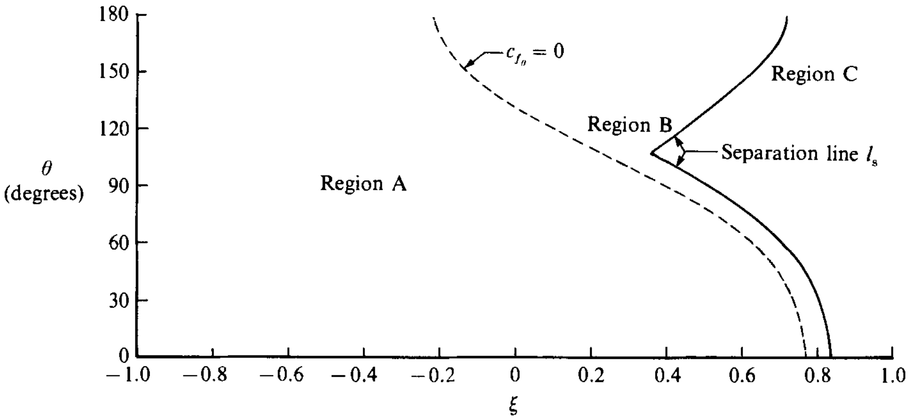

FIGURE 2. Typical flow regions on a prolate spheroid of thickness $t = \frac{1}{4}$ at $\alpha = 6°$ according to the calculations of Cebeci *et al.* (1981).

obtained at $\xi = \xi_0$ with initial conditions generated on either line of symmetry and continued in the circumferential direction. The marching procedure raises the question of a preferred direction and its role in the development of the numerical procedure. To elaborate this point further, consider laminar flow over the prolate spheroid of figure 1 at $\alpha = 6°$, for which figure 2 shows the separation lines and the line on which the circumferential skin-friction coefficient c_{f_θ} is zero as computed by Cebeci *et al.* (1981). In the region upstream of the line of zero c_{f_θ} (Region A) all u- and w-velocities are positive; in the region between this line and the two separation lines (Region B), u is positive and w is negative near the surface; and in the region downstream of the separation lines (Region C) u and w are negative near the surface and positive away from the surface.

The boundary-layer calculations can be performed in Regions A and B for a prescribed pressure distribution because the flow is attached and solutions can be obtained with initial conditions started on either line of symmetry. In Region A, however, it is logical to initiate the calculations on the windward line because the crossflow velocity is in the marching direction whereas the crossflow direction will be opposite to the marching direction if they originate on the leeward line. In the former case, the solutions can be obtained by a standard numerical procedure such as those of Crank & Nicolson (1947) or Keller (1974) and, in the latter case, a special numerical method is required to march in the direction opposite to that of the flow. The characteristic box was devised by T. Cebeci & K. Stewartson (1978, unpublished paper) to meet this requirement. It was used to obtain the results of figure 2, which are similar to those obtained by Wang (1975) and to those obtained with the zigzag numerical scheme by Cebeci *et al.* (1981) on the same finite-difference mesh. It was noted, however, that the solutions exhibited a tendency to oscillate as Region C was approached and further calculations with different meshes were performed with similar results. The investigation made clear the need for a means of assessing the accuracy and this, in turn, suggested a need for a criterion by which the mesh could be chosen by the numerical scheme so as to guarantee the required accuracy. A similar sequence of arguments followed from the examination of unsteady boundary layers with large flow reversal, Cebeci (1986*b*), for which a relationship of time interval to step length was identified as crucial to numerical accuracy and a criterion was established and used together with a form of the characteristic-box scheme. As a result, accurate results were obtained for the flow around a circular cylinder started impulsively from rest and numerical difficulties were not encountered even in regions of very large flow reversal.

The present study of three-dimensional steady flows benefits from the unsteady-flow investigation described in the previous paragraph in that a stability criterion of similar form is introduced and used with the characteristic-box scheme to obtain accurate and reliable solutions throughout the region of negative crossflow, Region B of figure 2. As we shall see in §5, the stability criterion required values of step lengths in both directions which were much smaller than those used by Cebeci *et al.* (1981) and the upper and lower 'separation lines' of figure 2 are altered, with important differences in the flow structure.

The three-dimensional equations are formulated in the following section in the manner required by the characteristic-box scheme of §3 which has been improved in several respects. Section 4 reports experiments performed to determine the consequence of the stability criterion and §5 presents new results for the flow over a prolate spheroid with thickness ratio of $\frac{1}{4}$ at an incidence of 6°. The emphasis is on Region B where the circumferential flow velocity is negative and on the identification of the boundary between Regions B and C. The paper ends with a summary of the more important conclusions.

2. Formulation

Since this paper extends the work of Cebeci *et al.* (1980, 1981) the notation and formulation are similar. The boundary-layer equations and their boundary conditions for an incompressible laminar flow in a curvilinear orthogonal coordinate system appropriate to a prolate spheroid at incidence (figure 1) may be written as

continuity:

$$\frac{\partial}{\partial \xi}(h_2 u)+\frac{\partial}{\partial \theta}(h_1 w)+\frac{\partial}{\partial y}(h_1 h_2 v) = 0; \tag{2}$$

x-momentum:

$$\frac{u}{h_1}\frac{\partial u}{\partial \xi}+\frac{w}{h_2}\frac{\partial u}{\partial \theta}+v\frac{\partial u}{\partial y}+w^2 K_2 = -\frac{1}{\rho h_1}\frac{\partial p}{\partial \xi}+\nu\frac{\partial^2 u}{\partial y^2}; \tag{3}$$

θ-momentum:

$$\frac{u}{h_1}\frac{\partial w}{\partial \xi}+\frac{w}{h_2}\frac{\partial w}{\partial y}+v\frac{\partial w}{\partial y}-uwK_2 = -\frac{1}{\rho h_2}\frac{\partial p}{\partial \theta}+\nu\frac{\partial^2 w}{\partial y^2}; \tag{4}$$

$$y = 0, \quad u = v = w = 0$$

$$y \rightarrow \infty, \quad u \rightarrow u_e(x,\theta), \quad w \rightarrow w_e(x,\theta). \tag{5}$$

Here $\xi = x/a$, θ is the azimuthal angle and (u, w, v) are the velocity components parallel to the body surface in the meridional and azimuthal directions and normal to this surface, respectively. Further h_1, h_2 are metric coefficients defined by

$$h_1 = a\left[\frac{1+\xi^2(t^2-1)}{1-\xi^2}\right]^{\frac{1}{2}}, \quad h_2 = at(1-\xi^2)^{\frac{1}{2}}, \tag{6}$$

with t denoting the thickness ratio ($=b/a$) of the elliptic profile. The parameter K_2 is the geodesic curvature of the surface lines $\xi=$ constant given by

$$K_2=\frac{at\xi}{h_1h_2(1-\xi^2)^{\frac{1}{2}}}. \tag{7}$$

As in Cebeci *et al.* (1981), the velocity components u_e and w_e are obtained from inviscid theory as

$$\frac{u_e}{u_\infty}=V_0(t)\cos\alpha\cos\beta-V_{90}(t)\sin\alpha\sin\beta\cos\theta, \tag{8a}$$

$$\frac{w_e}{u_\infty}=V_{90}(t)\sin\alpha\sin\theta. \tag{8b}$$

Here β denotes the angle between the line tangent to the elliptic profile and the positive-ξ axis and is given by

$$\cos\beta=\frac{(1-\xi^2)^{\frac{1}{2}}}{[1+\xi^2(t^2-1)]^{\frac{1}{2}}} \tag{9}$$

with the parameters $V_0(t)$ and $V_{90}(t)$ defined as

$$V_0(t)=\frac{(1-t^2)^{\frac{3}{2}}}{(1-t^2)^{\frac{1}{2}}-\frac{1}{2}t^2\ln\left\{\dfrac{1+(1-t^2)^{\frac{1}{2}}}{1-(1-t^2)^{\frac{1}{2}}}\right\}},\quad V_{90}(t)=\frac{2V_0(t)}{2V_0(t)-1}. \tag{10a,b}$$

To avoid the singularity at the nose ($\xi=-1$) we use the procedure of Cebeci *et al.* (1980) which employs transformations to solve the boundary-layer equations. Once the solutions are established for $-1\leqslant\xi\leqslant\xi_0$, calculations can be continued for $\xi>\xi_0$ in the above coordinate system.

The solution of the equations for $\xi>\xi_0$ is obtained with the equations expressed in terms of the dimensionless independent variable η, that is

$$\eta=\left(\frac{u_0}{\nu s}\right)^{\frac{1}{2}}y,\quad\text{with } s=\int_{-1}^{\xi}h_1\,\mathrm{d}\xi, \tag{11}$$

and the following dimensionless functions:

$$\frac{u}{u_0}=f(\xi,\theta,\eta),\quad\frac{w}{u_0}=g(\xi,\theta,\eta),\quad e(\xi,\theta,\eta)=\frac{\eta f}{2s}-\frac{v}{(u_0\nu s)^{\frac{1}{2}}}. \tag{12a, b}$$

With (11) and (12), a prime denoting differentiation with respect to η, and $\beta_1=K_2-\frac{1}{2}s$, (2)–(5) can be written as

$$e'+\beta_1f=\frac{1}{h_1}\frac{\partial f}{\partial\xi}+\frac{1}{h_2}\frac{\partial g}{\partial\theta}, \tag{13}$$

$$f''+sf'e-sK_2g^2+s\beta_2=s\left(\frac{f}{h_1}\frac{\partial f}{\partial\xi}+\frac{g}{h_2}\frac{\partial f}{\partial\theta}\right), \tag{14}$$

$$g''+sg'e+sK_2fg+s\beta_3=s\left(\frac{f}{h_1}\frac{\partial g}{\partial\xi}+\frac{g}{h_2}\frac{\partial g}{\partial\theta}\right), \tag{15}$$

$$\eta=0,\quad f=g=e=0, \tag{16a}$$

$$\eta\rightarrow\eta_e,\quad f\rightarrow\frac{u_e}{u_0}=\bar{u}_e,\quad g\rightarrow\frac{w_e}{u_0}=\bar{w}_e. \tag{16b}$$

Here β_2 and β_3 are pressure gradient parameters defined by

$$\beta_2 = \left(\frac{\bar{u}_\mathrm{e}}{h_1}\frac{\partial \bar{u}_\mathrm{e}}{\partial \xi} - \frac{\bar{w}_\mathrm{e}}{h_2}\frac{\partial \bar{u}_\mathrm{e}}{\partial \theta} + \bar{w}_\mathrm{e}^2 K_2\right), \quad \beta_3 = \left(\frac{\bar{w}_\mathrm{e}}{h_2}\frac{\partial \bar{w}_\mathrm{e}}{\partial \theta} - K_2 \bar{w}_\mathrm{e} \bar{u}_\mathrm{e}\right). \tag{17}$$

Equations (13)–(15) are valid everywhere except at $\theta = 0$, π where $g = 0$ which makes (15) singular. To obtain solutions for this special case, we differentiate (15) with respect to θ and set $g = 0$ in (13)–(15). We also define

$$G(\xi, \eta) = \frac{\partial g}{\partial \theta} \tag{18}$$

so that (13)–(16) can be written as

$$e' + \beta_1 f = \frac{1}{h_1}\frac{\partial f}{\partial \xi} + \frac{1}{h_2} G, \tag{19}$$

$$f'' + sf'e + s\beta_1 = s\frac{f}{h_1}\frac{\partial f}{\partial \xi}, \tag{20}$$

$$G'' + sG'e + sK_2 fG + s\beta_4 = s\frac{f}{h_1}\frac{\partial G}{\partial \xi}, \tag{21}$$

$$\eta = 0, \quad f = G = e = 0, \tag{22a}$$

$$\eta \to \eta_\mathrm{e}, \quad f = \bar{u}_\mathrm{e}, \quad G = \frac{\partial \bar{w}_\mathrm{e}}{\partial \theta}. \tag{22b}$$

Here β_4 is another pressure-gradient parameter defined by

$$\beta_4 = -K_2 \bar{u}_\mathrm{e} \frac{\partial \bar{w}_\mathrm{e}}{\partial \theta}. \tag{23}$$

3. Numerical method

Solutions to the conservation equations of the previous section have been obtained with the standard-box method of Keller in regions of positive crossflow velocity and the characteristic box in the presence of negative crossflow velocity. Details of the two methods are available, for example in Bradshaw, Cebeci & Whitelaw (1981) for three-dimensional flows. The accuracy of the solutions in regions with negative crossflow is strongly dependent on the choice of the finite-difference net, as discussed by Cebeci (1986*b*) and Cebeci, Khattab & Schimke (1987) for two-dimensional unsteady flows, and as shown here for three-dimensional steady flows.

The characteristic-box scheme is based on the solution of the boundary-layer equations along the local streamlines. If we denote the streamline direction by ψ and the angle that it makes with the ξ-axis by α, we can write (14) and (15) as

$$f'' + sf'e - sK_2 g^2 + s\beta_2 = \lambda \frac{\partial f}{\partial \psi}, \tag{24}$$

$$g'' + sg'e + sK_2 fg + s\beta_3 = \lambda \frac{\partial g}{\partial \psi}, \tag{25}$$

where

$$\lambda = s\left[\left(\frac{f}{h_1}\right)^2 + \left(\frac{g}{h_2}\right)^2\right], \quad \alpha = \tan^{-1}\left(\frac{h_1}{h_2}\frac{g}{f}\right). \tag{26}$$

Keller's method requires that (13), (24) and (25) are expressed as a first-order system and, for this purpose, we define

$$f' = n, \quad g' = m, \tag{27a, b}$$

and write (24) and (25) as

$$n' + sne - sK_2 g^2 + s\beta_2 = \lambda \frac{\partial f}{\partial \psi}, \quad m' + sme + sK_2 fg + s\beta_3 = \lambda \frac{\partial g}{\partial \psi}. \tag{27c, d}$$

The solution of the system given by (13), (27), subject to the boundary conditions in (16), by the standard-box or characteristic-box schemes depends on the difference equations for (27c, d); the remaining equations are unchanged. To discuss the details of the procedure for the characteristic-box scheme, let us consider a net given by

$$\left.\begin{aligned} &\xi_0 = 0, \quad \xi_i = \xi_{i-1} + k_i, \quad i = 1, 2, \ldots, I, \\ &\theta_0 = 0, \quad \theta_k = \theta_{k-1} + r_k, \quad k = 1, 2, \ldots, K, \\ &\eta_0 = 0, \quad \eta_j = \eta_{j-1} + h_j, \quad j = 1, 2, \ldots, J. \end{aligned}\right\} \tag{28}$$

With the notation show in figure 3, the difference equations for (27a, b) are obtained by averaging about the midpoint $(\xi_i, \theta_k, \eta_{j-\frac{1}{2}})$,

$$h_j^{-1}(f_j^{i,k} - f_{j-1}^{i,k}) = n_{j-\frac{1}{2}}^{i,k}, \quad h_j^{-1}(g_j^{i,k} - g_{j-1}^{i,k}) = m_{j-\frac{1}{2}}^{i,k}, \tag{29a, b}$$

where, for example,

$$n_{j-\frac{1}{2}}^{i,k} = \tfrac{1}{2}(n_j^{i,k} + n_{j-1}^{i,k}), \tag{30}$$

The difference approximations to (13) are obtained by centring all quantities except e at the centre of a cube $(\xi_{i-\frac{1}{2}}, \theta_{k-\frac{1}{2}}, \eta_{j-\frac{1}{2}})$ by taking the values of each parameter, say q, at the four corners of the box; that is,

$$q_{j-\frac{1}{2}}^{i-\frac{1}{2},k} = \tfrac{1}{2}(q_j^{i-\frac{1}{2},k} + q_{j-1}^{i-\frac{1}{2},k}) = \tfrac{1}{4}(q_j^{i,k} + q_j^{i-1,k} + q_{j-1}^{i,k} + q_{j-1}^{i-1,k}), \tag{31a}$$

and e is centred by writing it as

$$e_{j-\frac{1}{2}}^{i-\frac{1}{2},k-\frac{1}{2}} = \tfrac{1}{2}(e_j^{i-\frac{1}{2},k-\frac{1}{2}} + e_{j-1}^{i-\frac{1}{2},k-\frac{1}{2}}). \tag{31b}$$

The unknown parameters of (31) correspond to $q^{i,k}$ and $e_j^{i-\frac{1}{2},k-\frac{1}{2}}$ so that, when a solution of the system given by (13) and (27) is obtained, f, g, n and m are computed at (i, k, j) and e at $(i-\frac{1}{2}, k-\frac{1}{2}, j)$. This modified centring procedure is necessary to avoid oscillations which can arise from the use of (13) rather than the stream function, as discussed by Cebeci (1986c). With this notation, (13) can be written in the form

$$h_j^{-1}(e_j - e_{j-1}) + \bar{\beta}_1 \bar{f}_{j-\frac{1}{2}} = \overline{h_1^{-1}}\, k_I^{-1}(\bar{f}_i - \bar{f}_{i-1}) + \overline{h_2^{-1}}\, r_k^{-1}(\bar{g}_k - \bar{g}_{k-1}), \tag{32}$$

where, for example,

$$\left.\begin{aligned} &e_j = e_j^{i-\frac{1}{2},k-\frac{1}{2}}, \quad \bar{f}_j = \tfrac{1}{2}(f_j^{i-\frac{1}{2},k} + f_j^{i-\frac{1}{2},k-1}), \\ &\bar{f}_i = \tfrac{1}{2}(f_j^{i,k-\frac{1}{2}} + f_{j-1}^{i,k-\frac{1}{2}}), \quad \bar{g}_k = \tfrac{1}{2}(g_j^{i-\frac{1}{2},k} + g_{j-1}^{i-\frac{1}{2},k}), \\ &\bar{\beta}_1 = (\beta_1)^{i-\frac{1}{2},k-\frac{1}{2}}. \end{aligned}\right\} \tag{33}$$

Equations (27c, d) are similar so we shall consider only (27c), which at point B is given by

$$\begin{aligned} &\tfrac{1}{2}h_j^{-1}(n_j^{i,k} - n_{j-1}^{i,k}) + \tfrac{1}{2}h_j^{-1}(n_j^{i-1,l} - n_{j-1}^{i-1,l}) + \bar{s}\tfrac{1}{2}(n_{j-\frac{1}{2}}^{i,k} + n_{j-\frac{1}{2}}^{i-1,l})\, e_{j-\frac{1}{2}}^{B} \\ &\quad - (\overline{sK_2})\tfrac{1}{2}[(g^2)_{j-\frac{1}{2}}^{i,k} + (g^2)_{j-\frac{1}{2}}^{i-1,l}] + (\overline{s\beta_1}) = \tfrac{1}{2}(\lambda_{j-\frac{1}{2}}^{i,k} + \lambda_{j-\frac{1}{2}}^{i-1,l})\, \frac{(f_{j-\frac{1}{2}}^{i,k} - f_{j-\frac{1}{2}}^{i-1,l})}{\Delta\psi_{j-\frac{1}{2}}}, \end{aligned} \tag{34}$$

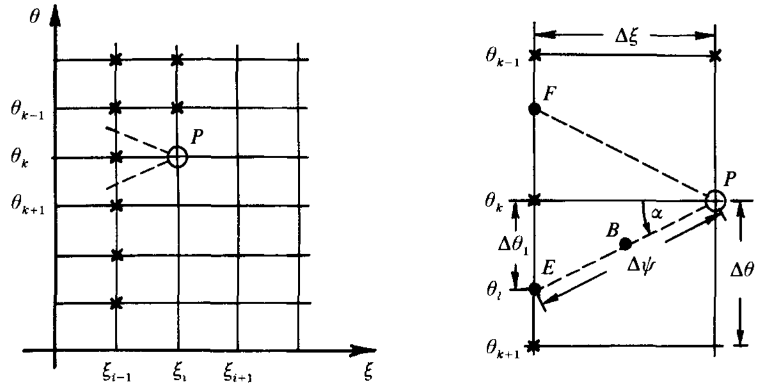

FIGURE 3. Finite-difference notation for the characteristic-box scheme: ○, unknown; ×, known.

where the relation between e_j^B and $e_j^{i-\frac{1}{2},\,k-\frac{1}{2}}$ is

$$e_j^B = \frac{e_j^{i-\frac{1}{2},\,k-\frac{1}{2}} - e_j^{i-\frac{1}{2},\,k-\frac{3}{2}}}{\theta_{k-\frac{1}{2}} - \theta_{k-\frac{3}{2}}}(\theta_B - \theta_{k-\frac{1}{2}}) + e_j^{i-\frac{1}{2},\,k-\frac{1}{2}}. \tag{35}$$

The boundary conditions follow from (16) and can be written as

$$f_0 = g_0 = e_0 = 0; \quad f_J = \bar{u}_e, \quad g_J = \bar{w}_e. \tag{36}$$

The algebraic system given by (29*a*, *b*), (32), (34), and that resulting from (27*d*), together with the boundary conditions given by (36) is nonlinear. Linearization is achieved with Newton's method and the equations are solved by the block-elimination method described, for example, in Cebeci & Bradshaw (1984).

4. Accuracy and stability requirements of the characteristic-box scheme; region of positive crossflow

As discussed by Keller (1974), the box method is second-order accurate and unconditionally stable. While the accuracy of the standard box is well established for flows without backflow, that of the characteristic box and its dependence on the choice of the net in the circumferential and streamwise directions has not been explored for flows with and without backflow. The use of the characteristic-box scheme in regions where there is no flow reversal allows its accuracy and sensitivity to the choice of net spacings to be examined by comparing results with those obtained with the standard box.

The positive crossflow of the prolate spheroid, Region A of figure 1, is ideal for this purpose since accurate solutions can be obtained with the standard-box scheme by marching from the windward line of symmetry to the leeward line of symmetry and the results compared with those of the characteristic box in which the solutions are obtained by marching from the leeward line of symmetry to the windward line of symmetry. This is examined further with the net shown in figure 3 at a given distance y from the surface and with the assumption that the solutions originate on the leeward line of symmetry; the symbol × denotes the location where the solution is known and the symbol ○ denotes the location where the solution is to be found. The backward characteristic from point P is in the local streamline direction and intersects the ξ_{i-1} line at E when there is a positive crossflow velocity and at F when

	Standard box		Characteristic box			
$\theta \backslash \Delta\xi$	0.20	0.025	0.20	0.10	0.05	0.025
0	0.72019	0.71099	0	0	0.71155	0.71099
20	0.71216	0.70537	0	0	0.70780	0.70655
40	0.69604	0.68662	0	0	0.69070	0.68857
60	0.66827	0.65592	0	0	0.66151	0.65857
80	0.62998	0.61422	0	0	0.62066	0.61746
100	0.58312	0.56432	0	0	0.57106	0.56777
120	0.53246	0.51172	0	0	0.51765	0.51490
140	0.48600	0.46576	0.39190	0.45759	0.47025	0.46824
145	0.47717	0.45887	0.50591	0.46903	0.46088	0.45923
150	0.46765	0.44890	0.43355	0.45433	0.45256	0.45083
155	0.46091	0.44461	0.45830	0.44870	0.44595	0.44466
160	0.45384	0.43708	0.43890	0.44269	0.44021	0.43883
180	0.46462	0.43076	0.46462	0.43924	0.43229	0.43076

TABLE 1. Streamwise wall shear parameter f''_w computed with standard and characteristic box schemes at $\xi = -0.50$

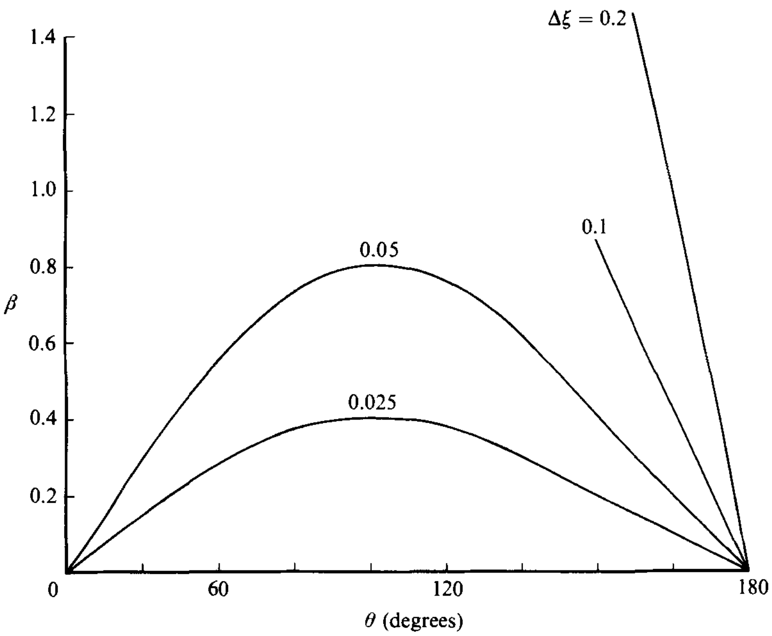

FIGURE 4. Effect of streamwise spacing $k_1 (\equiv \Delta\xi)$ on the variation of the stability parameter β in the circumferential direction.

the crossflow velocity is negative. Since the characteristic box computes the region *EFP*, which is known as the domain of dependence of point *P*, it ensures that necessary information reaches point *P* from region *EFP*. It is important that the domain of stable computations can be determined *a priori* and this is achieved by determining the ratio $\beta (\equiv \Delta\theta_1 / \Delta\theta)$, which is also equal to $(w/u)(h_1/h_2)(\Delta\xi/\Delta\theta)$, and requiring that it remains small during the calculations: we shall refer to this requirement as the stability criterion of the characteristic box.

Table 1 shows the computed streamwise wall-shear values and figure 4 the variations of the stability parameter β at $\xi = -0.50$ with initial conditions generated at $\xi_0 = -0.90$ for uniform 5° increments in θ and for four different uniform step lengths ξ corresponding to 0.20, 0.10, 0.05 and 0.025. The solutions of the standard box were obtained by starting the calculations on the windward line of symmetry and marching towards the leeward line. The solutions of the characteristic box, on the other hand, were obtained with calculations originating on the leeward line of symmetry and marching towards the windward direction. The results show that the accuracy of the solutions of the standard box are not sensitive to the $\Delta\xi$-spacings used in the calculations but those with the characteristic box are. For the $\Delta\xi$-spacings of 0.20 and 0.10, the results of figure 4 indicate that the stability parameter β increases rapidly with breakdown of the solutions at $\theta = 120°$. With step lengths of 0.05 and 0.025, the calculations proceed without breakdown and with the expected lower values of β. Whereas those obtained with two coarse grids show oscillations in θ, those with the finer grids do not.

The results in table 1 also indicate that the accuracy of the solutions of the characteristic-box scheme are comparable with those of the standard-box scheme. For example, with $\Delta\xi = 0.025$ the maximum difference between values of f''_w computed by the two numerical schemes is 0.00324 and occurs at $\theta = 80$ where β is maximum. The difference is smaller at other values of θ, where β is less than its maximum value and could be further reduced with β less than 0.40. These results show that the accuracy of the characteristic box is the same as that of the standard box provided that the grid is appropriate and that the stability parameter β is a measure of the numerical accuracy.

5. Region of negative crossflow

Having established the accuracy of the characteristic box scheme and its stability requirements, we now turn our attention to the behaviour of flow in region B and to the identification of its boundaries with region C. It is expected that the calculations must be performed with care since the accuracy of the solutions has been shown to depend on the choice of the net in the circumferential and streamwise directions. For this reason it is useful to identify three subregions in which to perform the calculations. The first subregion starts at ξ_A where the w-velocity becomes negative and extends to ξ_B where the streamwise wall shear f''_w vanishes. According to figure 2 and to the previous calculations of Cebeci *et al.* (1981), this region corresponds to $-0.2 \leqslant \xi \leqslant 0.35$, although these limits need to be determined more accurately. The second and third subregions begin at the first separation point ξ_B and are bounded by the leeward line of symmetry and the upper 'separation' line and by the windward line of symmetry and the lower 'separation' line, respectively.

5.1. *The first subregion*

With initial conditions given at ξ_A, the calculations were started at the next specified ξ-location on the line of symmetry and continued towards the leeward line of symmetry with the standard box scheme in regions where w is positive and the characteristic box scheme where w is negative. Uniform step lengths of 2.5° in the circumferential direction, as in Cebeci *et al.* (1981), and several non-uniform step lengths (different grids are designated by roman numerals) in the streamwise direction, as summarized in table 2, were used to investigate the role of the stability criterion.

Figures 5 and 6 show the results obtained with grid I. Figure 5(*a*) shows the

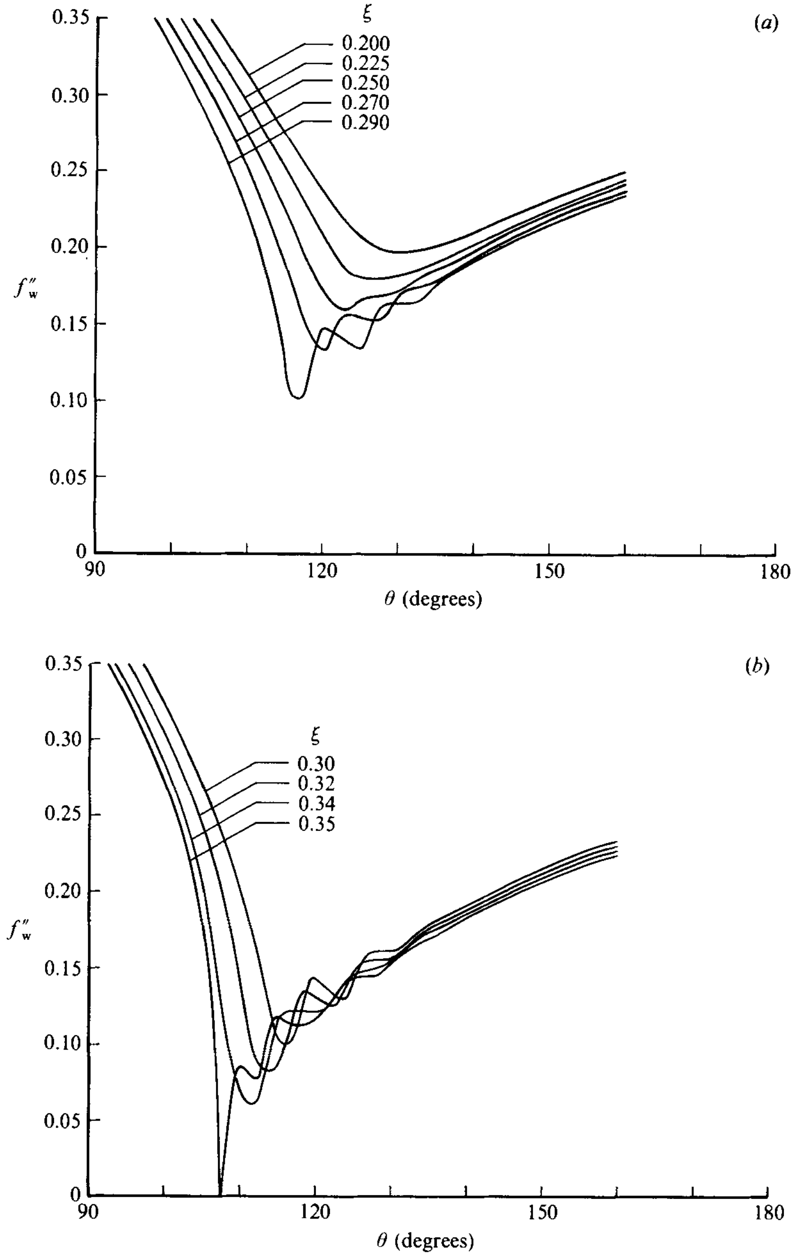

FIGURE 5. Variation of streamwise wall-shear parameter f''_w in the circumferential direction computed with grid I.

variation of the streamwise wall-shear parameter f''_w with θ for several values of ξ. As can be seen, for values of $\xi = 0.200$ and 0.225, the solutions are smooth and free of oscillations. A slight oscillation occurs around $\theta = 125°$ for $\xi = 0.250$ and increases substantially, covering a range of θ from 120° to 135°, at $\xi = 0.270$, after which the solutions are smooth and free of wiggles. The situation worsens for subsequent values of $\xi < 0.30$, but solutions do not break down in spite of the oscillations covering a larger region until they become smooth around $\theta = 135°$. At $\xi = 0.30$, the solutions

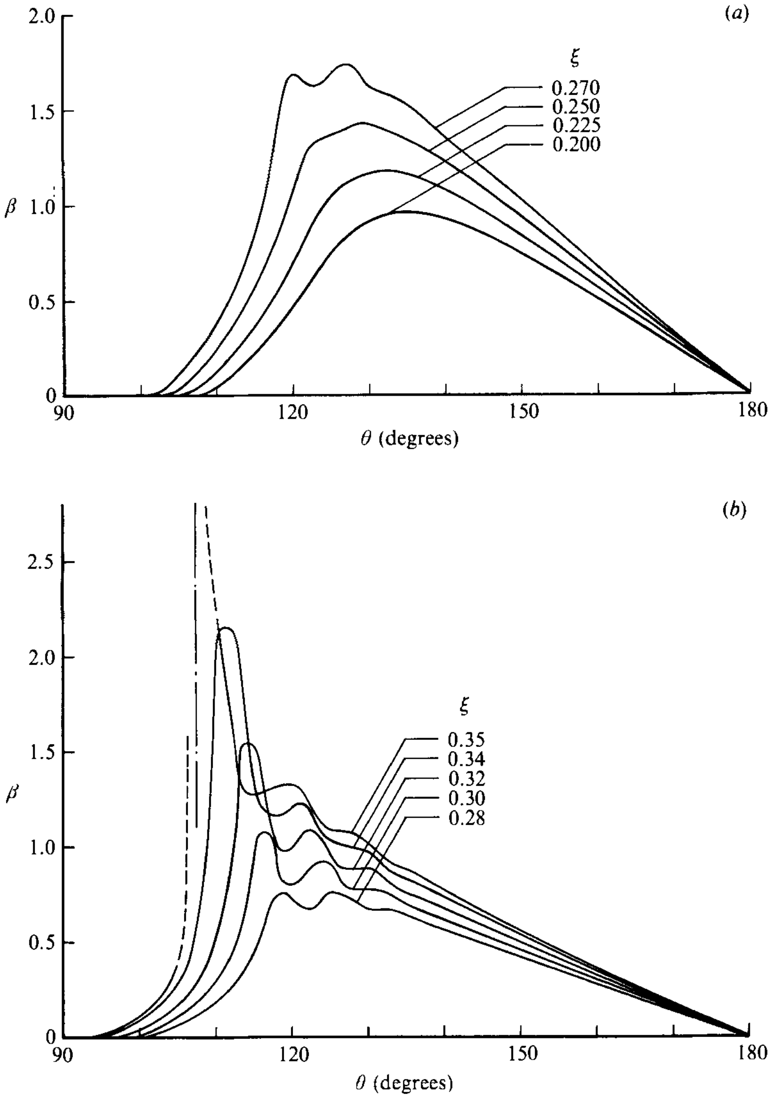

FIGURE 6. Effect of Grid I on the variation of the stability parameter β in the circumferential direction.

do not converge and cause the calculations to terminate. With solutions available for $\xi < 0.30$, calculations at higher values were started on the leeward line of symmetry and continued towards the windward line of symmetry. As shown in figure 5(*b*), the solutions exhibit oscillations in the same region as those that originated from the windward line of symmetry but they do not break down until $\xi = 0.350$.

The cause of the oscillations was investigated by computing the maximum value of the stability parameter β at each θ-station at a given ξ-location and figure 6 shows the results for several values of ξ. We note from figure 6(*a*) that β increases with increasing ξ, and attains a maximum value at $\xi = 0.27$ which is about 70% bigger than its maximum value at $\xi = 0.20$. The solutions for β also exhibit oscillations at the same value of ξ as f''_w. Figure 6(*b*) shows that, as the value of the stability parameter β increases further with increasing ξ, the oscillations worsen so that the

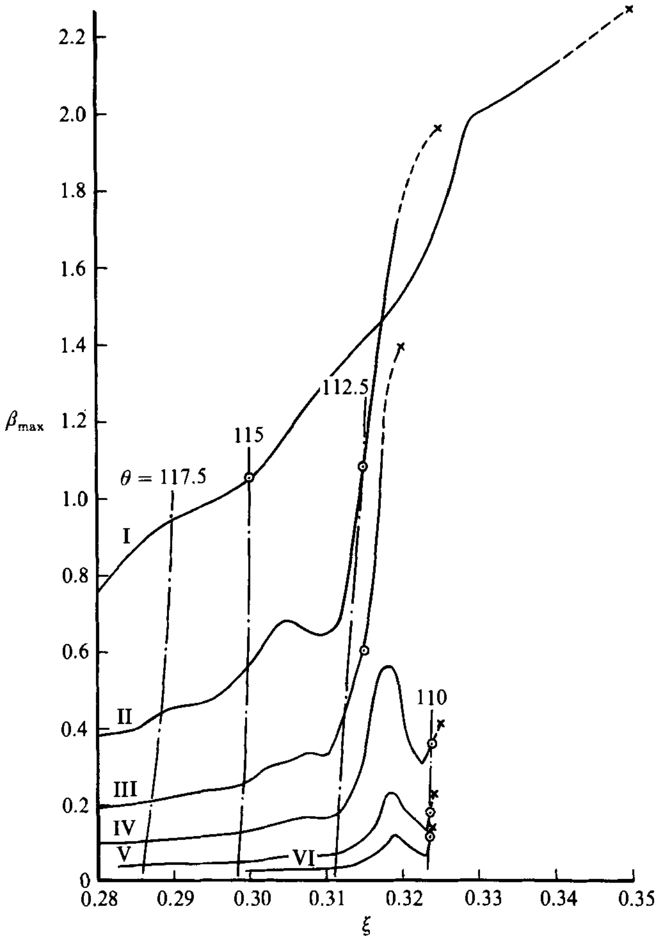

FIGURE 7. Effect of grid on the variation of the stability parameter β with ξ. The symbols ○ and × denote the location of the breakdown of the solutions originated from the windward and leeward lines of symmetry, respectively.

accuracy of the solutions for values of ξ greater than 0.27 become increasingly suspect.

Since the solutions obtained with Grid I were acceptable up to $\xi = 0.270$, the subsequent calculations, with the grids of table 2, began at this value. Figure 7 shows the variation of the stability parameter β for six grids in which the $\Delta\xi$-spacing diminishes from I to VI and, as expected, a decrease in the $\Delta\xi$-spacing decreases the maximum value of β. Figure 8 shows the effect of $\Delta\xi$-spacing on the computed values of f''_w at $\xi = 0.30$ and we note from figure 7 that β exceeds unity at this ξ-station with Grid I and the solutions of figure 8(*a*) oscillate as a result. With Grid III, however, the maximum value of β decreases to 0.27 and the solutions improve considerably (figure 8*a*); with the further refinement of Grid VI, the value of β at $\xi = 0.30$ drops from 0.27 to 0.028 and the solutions of figure 8(*b*) are smooth.

Figures 9, 10 and 11 show the variation of f''_w with θ for conditions approaching flow separation. Figure 9 shows that the solutions computed with Grids V and VI are the same at $\xi = 0.315$ and that they contain no oscillations, although a rapid decrease occurs in f''_w around $\theta = 112.5°$ and is followed by a sharp increase and

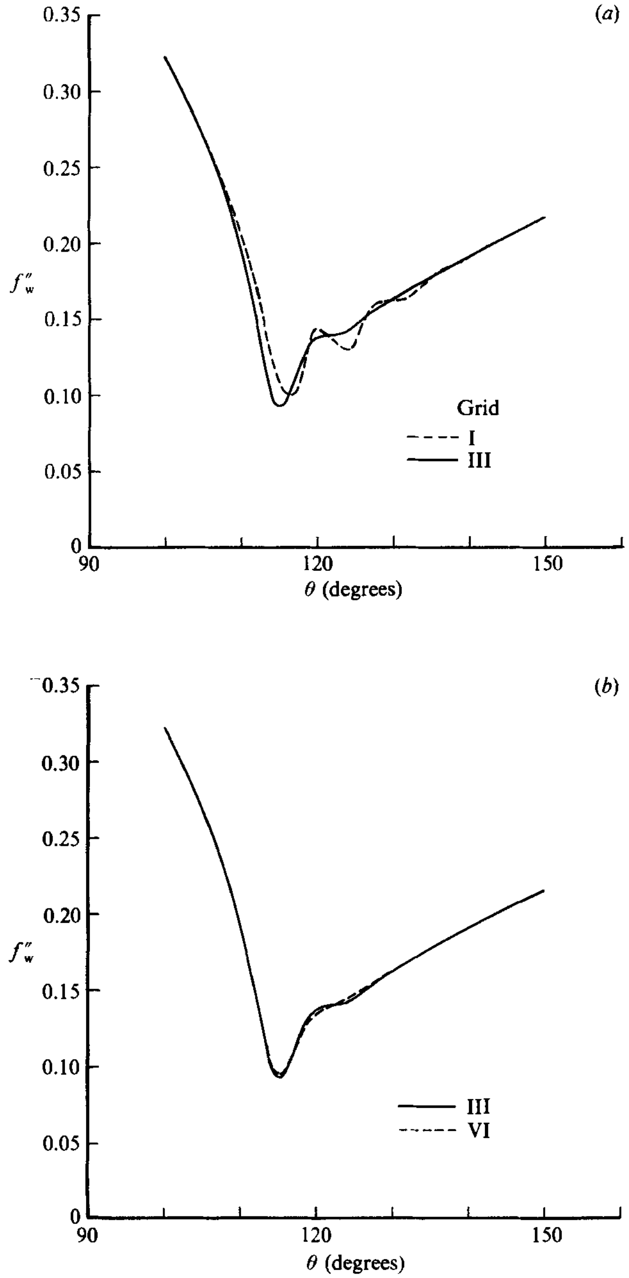

FIGURE 8. Effect of grid on the variation of the streamwise wall-shear parameter f''_w with θ at $\xi = 0.30$.

decrease and another continuous increase. The results in figure 10 exhibit a similar behaviour with Grid VI; again there are no oscillations in the solutions but the dip in f''_w moves towards the windward line of symmetry with increasing ξ and finally becomes negative at $\xi = 0.32375$. The results in figure 11 were obtained with a solution procedure slightly different from that used for figures 9 and 10. In one set of calculations, as in figures 9 and 10, the calculations (shown by the solid line) were

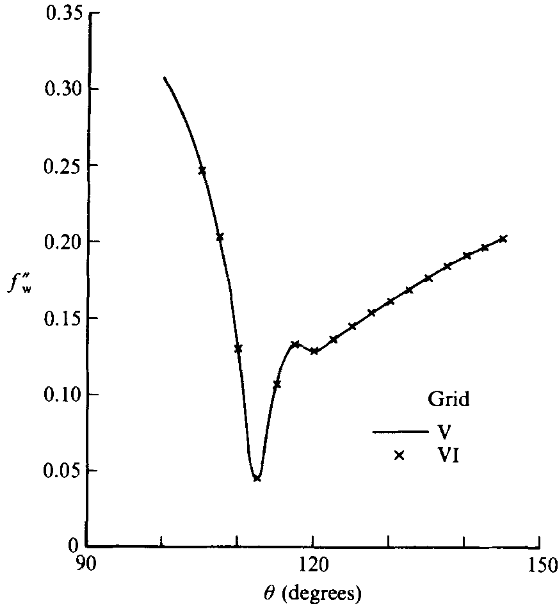

FIGURE 9. Variation of the streamwise wall-shear parameter f''_w with θ for Grids V and VI at $\xi = 0.315$.

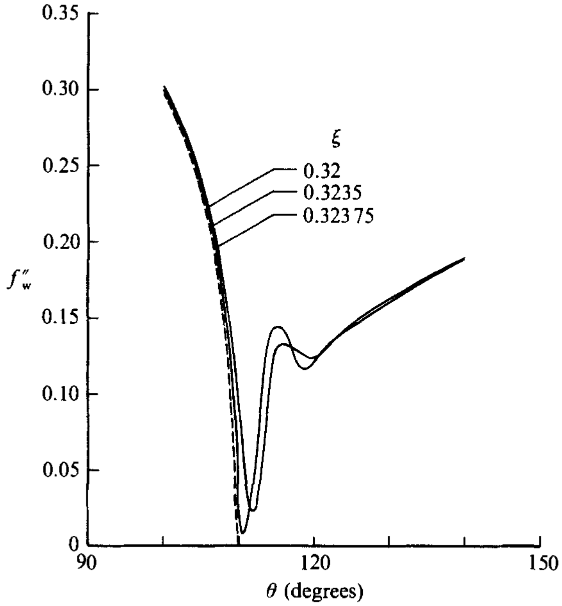

FIGURE 10. Variation of the wall-shear parameter f''_w with θ for Grid VI at three values of ξ.

performed with the characteristic-box scheme by marching from the leeward line of symmetry (LS) to the windward line of symmetry (WS). In a second set (shown by a dashed line) the standard-box scheme was used to march from the windward line of symmetry to $\theta = 110°$ and with the characteristic scheme from the leeward line of symmetry to the same location. For $\theta < 107°$, the results of the procedures agree with a maximum deviation between the f''_w values of less than 0.002. The deviation

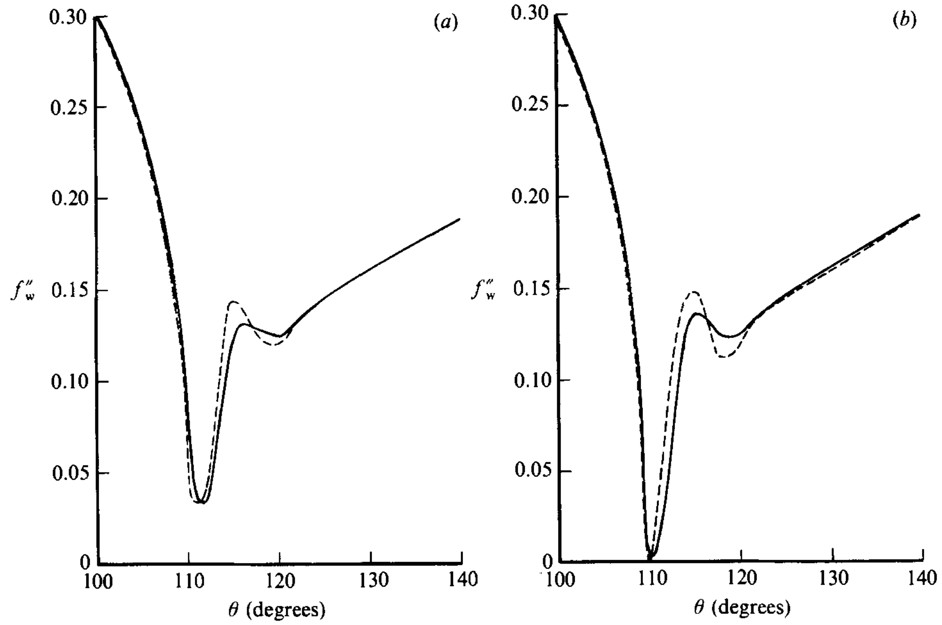

FIGURE 11. Effect of the marching direction on the variation of the wall shear parameter f''_w at (a) $\xi = 0.3225$, (b) $\xi = 0.32625$. Solid line denotes solutions from LS and dashed line those from WS for $\theta < 110°$ and LS for $\theta > 110°$.

increases, for $\theta > 107°$ with maximum values of 0.0140 at $\theta = 110°$ and 0.0208 at $\theta = 115°$. Examination of the magnitude of the stability parameter β indicates that the maximum value of β is less than 0.1 for $\theta < 107°$, but is 0.43 at $\theta = 112.5°$.

The use of different grids in the ξ-direction allows us to determine whether or not the stability criterion is satisfied and if there is a preferred direction of marching from one line of symmetry to another. We would expect that the solutions obtained by marching from either line of symmetry should be identical, but this was not the case when Grid I was used and the reason for it was that the stability criterion was not satisfied. Additional calculations with the grids of table 2 confirm that if the grid is chosen so that the stability parameter is relatively small, they break down at the same location regardless of which line of symmetry the solutions originate. With Grid III, and as shown in figure 7 and table 3, solutions originating from the windward and leeward line of symmetry break down at $\xi = 0.315$ and 0.32, respectively, even though the maximum value of β at $\xi = 0.315$ is around 0.6; this occurs because the solutions at previous ξ-stations have not satisfied the stability condition and allowed β to exceed unity. With Grid IV, solutions from windward and leeward symmetry lines break down at $\xi = 0.32375$ and $x = 0.325$, respectively, and closer examination of β (see figure 7) shows that the solutions obtained for previous values of ξ are more accurate than those that used Grids I and II. The solutions become even more accurate and lead to almost the same breakdown location if a more refined grid, like VI, is used, for now the two ξ-values are 0.3235 and 0.32375 at $\theta = 110°$.

It is clear from the above discussions that for a uniform grid in $\theta(\delta\theta = 2.5°)$, the solutions exhibit oscillations when the stability parameter β is large and that, with a proper choice of grid in ξ, the magnitude of β becomes smaller and the oscillations disappear. It is also clear that, at some ξ starting around 0.29, a small kink develops in the wall-shear parameter f''_w around $\theta = 113°$ and becomes more pronounced with

	$\Delta\xi$ variations					
ξ	I	II	III	IV	V	VI
0.1500–0.2500	0.0250	—	—	—	—	—
0.2500–0.2700	0.0200	—	—	—	—	—
> 0.2700	0.0100	—	—	—	—	—
0.1500–0.2750	—	0.01250	—	—	—	—
> 0.2750	—	0.00500	—	—	—	—
0.1600–0.2700	—	—	0.00500	—	—	—
> 0.2700	—	—	0.00250	—	—	—
0.1600–0.2000	—	—	—	0.00500	—	—
0.2000–0.2700	—	—	—	0.00250	—	—
> 0.2700	—	—	—	0.00125	—	—
0.1600–0.2000	—	—	—	—	0.00250	—
0.2000–0.2700	—	—	—	—	0.00125	—
> 0.2700	—	—	—	—	0.00050	—
0.1600–0.2000	—	—	—	—	—	0.00250
0.2000–0.2700	—	—	—	—	—	0.00125
0.2700–0.2820	—	—	—	—	—	0.00050
> 0.2820	—	—	—	—	—	0.00025

TABLE 2. Variable step lengths in the streamwise direction for the region $\xi_A \leqslant \xi \leqslant \xi_B$

Grid		ξ	θ (degrees)
I	○	0.30	115
	*	0.35	107.5
II	○	0.315	112.5
	*	0.325	110
III	○	0.315	112.5
	*	0.32	112.5
IV	○	0.32375	110
	*	0.325	110
V	○	0.3235	110
	*	0.3240	110
VI	○	0.3235	110
	*	0.32375	110

TABLE 3. Effect of grid on the marching direction. Calculation breakdown point at: ○ from windward side, * from leeward side

increasing ξ (see Figures 8*b*, 9, 10 and 11): it is still present with Grids V and VI even though the maximum value of β is less than 0.25. Further calculations were performed with variations in $\delta\theta$ in the range $106° \leqslant \theta \leqslant 128°$ to determine whether the kink was a feature of the grid. Table 4 shows the final calculation grid in which the $\Delta\xi$-spacing was the same as in Grid IV up to $\xi = 0.28$ and was varied for $\xi > 0.28$ as shown in table 5.

Figures 12 and 13 show the results obtained at $\xi = 0.30$, 0.315 and 0.3155 with the grids of tables 4 and 5 and that the kink of figures 8(*b*) and 9 has disappeared. As can be seen at $\xi = 0.315$, the variation in f''_w is very rapid near $\theta = 110°$, as the flow tends to separation, which first occurs at $\xi = 0.3155$ and $\theta = 110.25°$, as shown in figure 12(*c*). The solution there is remarkably smooth with no kinks except even a

θ (degrees)	r_k (degrees)	θ (degrees)	r_k (degrees)
0–65	5	109–111	0.25
65–72.5	4, 3.5	111–111.6	0.3
72.5–90	2.5	111.6–114	0.4
90–95	2, 1.5	114–125	0.5
95–105	1.25	125–128	0.75
105–106	1	128–137	1
106–107.5	0.75	137–152	1.5
107.5–108	0.5	152–160	2
108–108.4	0.4	160–180	2.5
108.4–109	0.3		

TABLE 4. Non-uniform grid in the circumferential direction for the region $-1 \leqslant \xi \leqslant \xi_B$ with step lengths in the streamwise direction corresponding to Grid IV up to $\xi = 0.28$ and to those in table 5 for $\xi > 0.28$

ξ	k_i
0.2800–0.2900	0.001
0.2900–0.2950	0.00075
0.2950–0.3100	0.0005
0.3100–0.3130	0.00020
0.3130–0.3151	0.00015
0.3151–0.3172	0.0001

TABLE 5. Grid in the ξ-direction for the non-uniform grid in table 4

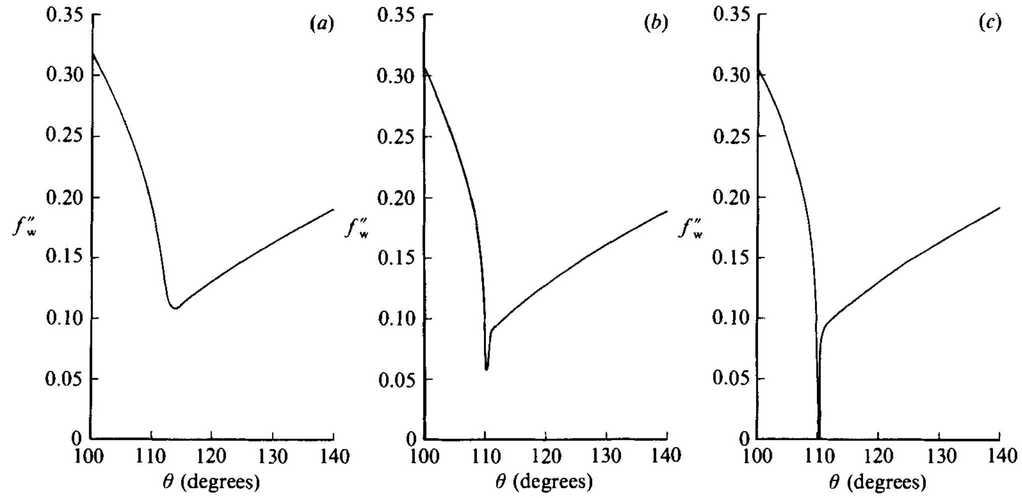

FIGURE 12. Effect of the non-uniform θ-grid on the variation of the streamwise wall shear f''_w at (a) $\xi = 0.30$, (b) 0.315, (c) 0.3155.

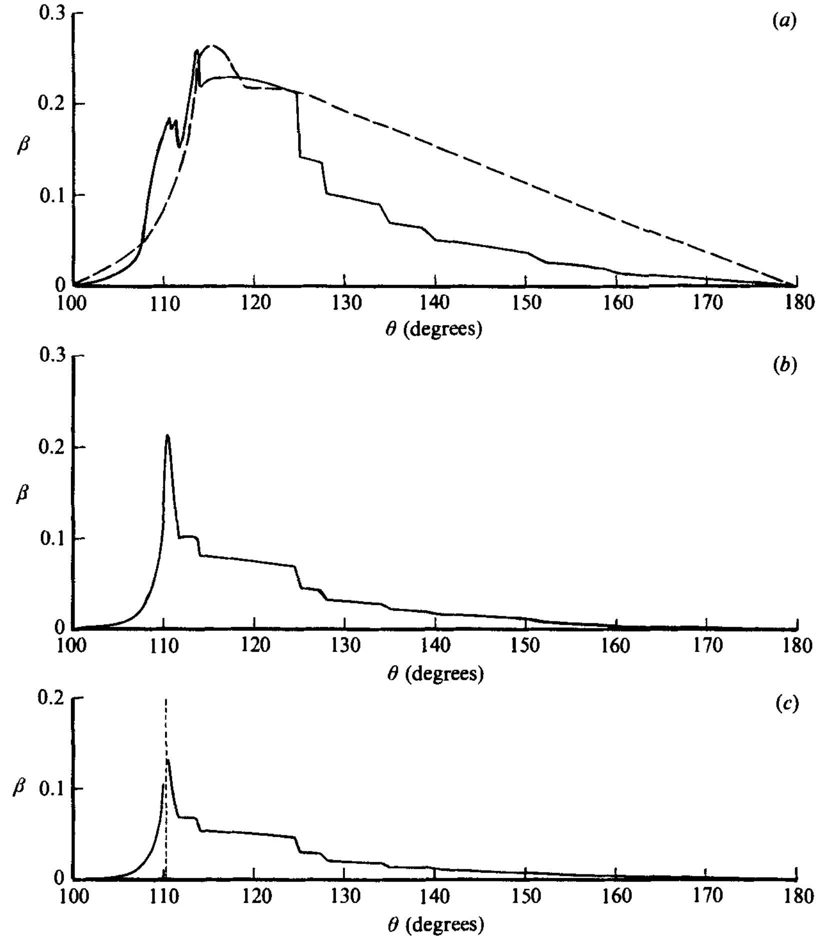

FIGURE 13. Variation of the stability parameter β (solid lines) for the results shown in figure 12. (*a*) $\xi = 0.30$, (*b*) 0.315, (*c*) 0.3155. Dashed line in (*a*) is for results in figure 8(*b*).

more rapid variation in f''_w around $\theta = 110°$. Figure 13 confirms that the stability parameter β at these three ξ-stations is small and it is interesting to note that its maximum value with the new non-uniform grid in figure 13(*a*) is practically the same as that obtained with uniform grid which led to the results of figure 8(*b*).

The behaviour of the displacement-thickness distributions in this first subregion are also of interest, and figure 14 shows the variation of the two components of the dimensionless displacement thicknesses $(\delta_x^*/s)\,R_s^{\frac{1}{2}}$ and $(\delta_\theta^*/s)\,R_s^{\frac{1}{2}}$. Here δ_x^* and δ_θ^* are defined by

$$\delta_x^* = \int_0^\infty \left(1-\frac{u}{u_e}\right)\mathrm{d}y = \frac{s}{R_s^{\frac{1}{2}}}\int_0^\infty \left(1-\frac{f}{f_e}\right)\mathrm{d}\eta, \tag{37a}$$

$$\delta_\theta^* = \int_0^\infty \left(1-\frac{w}{w_e}\right)\mathrm{d}y = \frac{s}{R_s^{\frac{1}{2}}}\int_0^\infty \left(1-\frac{g}{g_e}\right)\mathrm{d}\eta. \tag{37b}$$

The variations in δ_x^* and δ_θ^* with increasing θ are smooth except for a slight kink at $\theta = 110.25°$ shown as a dashed line on figure 14, and the magnitudes remain finite with $\mathrm{d}\delta^*/\mathrm{d}\theta$ becoming very large as the separation point is approached.

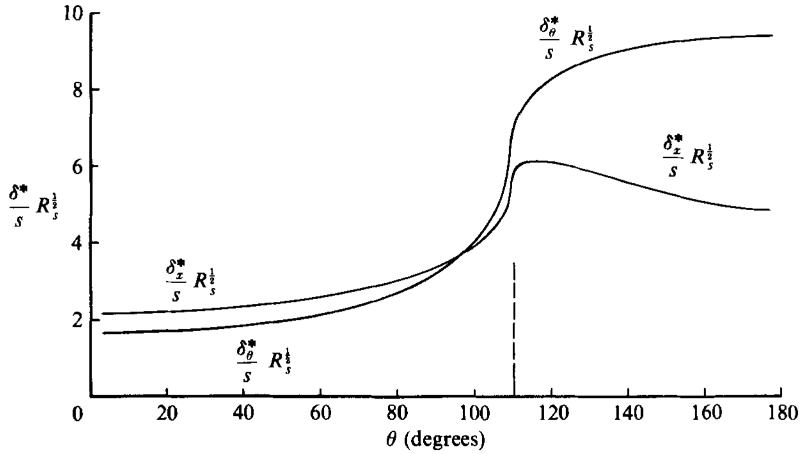

FIGURE 14. Variation of the dimensionless displacement thickness in the circumferential direction in the first subregion at $\xi = 0.3155$.

θ (degrees)	r_k (degrees)
135–129	1
129–124.5	1.25, 1.5, 1.75
124.5–114.5	1
114.5–113.2	1.3
113.2–112	1.2
112–110.75	1.25

TABLE 6. θ-grid for subregion $0.3172 \leqslant \xi \leqslant 0.7125$ with ξ-step lengths corresponding to those in table 7

5.2. *The second subregion*

The boundaries of the second subregion have been defined in part by the results of §5.1 which showed that the first flow separation occurred at $\xi = 0.3155$, rather than $\xi = 0.35$ as computed by Cebeci *et al.* (1981), and the separation on the leeward line of symmetry occurred at $\xi = 0.7125$. The calculations for the second subregion again made use of a non-uniform grid in the θ- and ξ-directions and it is evident that solutions from the leeward line of symmetry will terminate at $\theta = 110.25°$. Since the stability parameter β puts severe restrictions on the grid, we have chosen to use a coarser grid in the θ-direction after some ξ-station downstream of $\xi = 0.3155$ in order to take larger steps in the streamwise direction. For this purpose the calculations were performed with the non-uniform grid of table 4 up to $\xi = 0.3172$ after which a new θ-grid shown in table 6 was used for the region $110.75° < \theta < 135°$; for $\theta > 135°$, the θ-grid remained the same as in table 4.

Since $\theta = 110.75°$ is the last θ-station where the calculations can be performed in the subregion 2 with the grid of table 6, it is necessary to modify the numerical procedure at this θ-station. This was accomplished by replacing the interpolation procedure used to obtain the solutions at E of ξ_{i-1} (see figure 3) with an extrapolation procedure. Since the stability parameter β is small, this modification should not influence the accuracy of the solutions and this was verified by calculating up to $\xi = 0.3125$ with both procedures.

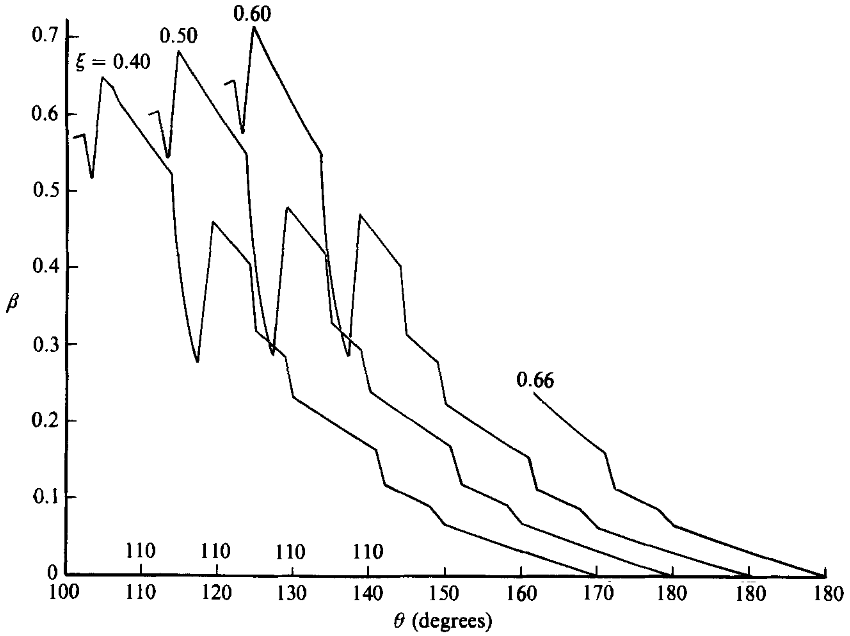

FIGURE 15. Variation of the stability parameter with θ in the second subregion.

ξ	k_i	ξ	k_i
0.3172–0.3180	0.00030, 0.00050	0.5200–0.5560	0.00075
0.3180–0.3240	0.00100	0.5560–0.6000	0.00050
0.3240–0.3600	0.00200	0.6000–0.6500	0.00040
0.3600–0.4500	0.00150	0.6500–0.6850	0.00025
0.4500–0.4900	0.00125	0.6850–0.7200	0.00050
0.4900–0.5200	0.00100	0.7200–0.7350	0.00100
		0.7350–0.8500	0.00125

TABLE 7. ξ-grid for subregions 2 and 3

Calculations with the grids of tables 6 and 7, figures 15–20, show that the stability parameter β remained small and led to solutions free of oscillations. We note from figure 15 that the value of β is relatively constant up to $\xi \leqslant 0.60$ with a maximum value of around 0.7 due to the coarse grid in the θ-direction. Figure 16 permits a comparison between the wall-shear values computed by the present method with those of Cebeci *et al.* (1981) whose solutions with Grid I oscillate as they approach $\theta = 110.25°$ and cause the wall shear to vanish. The θ-location where this occurs increases with ξ and leads to the upper 'separation' line indicated in figure 2. The present solutions do not oscillate, approach $\theta = 110.25°$ smoothly and remain finite. It is interesting to note also that in the absence of oscillations, both solutions agree well with each other.

Figures 17 and 18 show the variation of f''_w with ξ and θ for several values of θ and ξ, respectively. We note from figure 17 that the variation of f''_w for $\theta = 110.75$ and $\xi \leqslant 0.3155$ is similar to that at $\theta = 110.25$ for which separation occurs first at $\xi_s = 0.3155$. At this ξ_s-value, the trend of f''_w, as expected, changes from the one

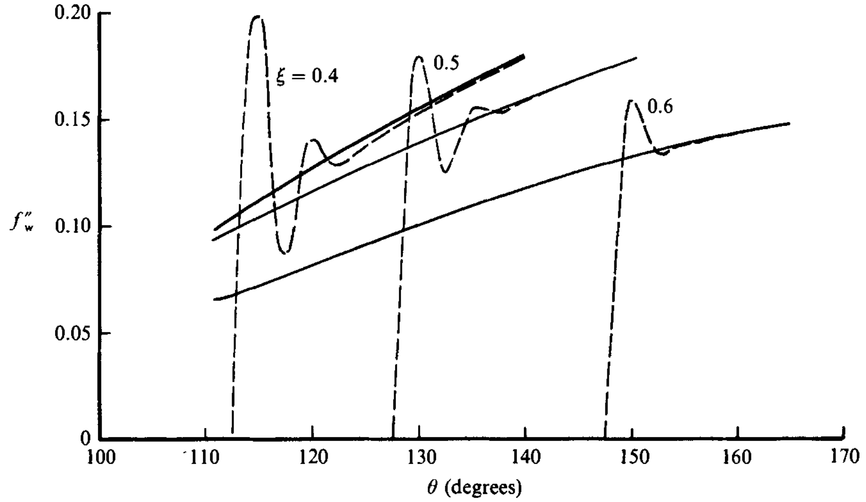

FIGURE 16. Comparison between the wall-shear values computed by the present method (solid line) and the method of Cebeci *et al.* (1981) (dashed line).

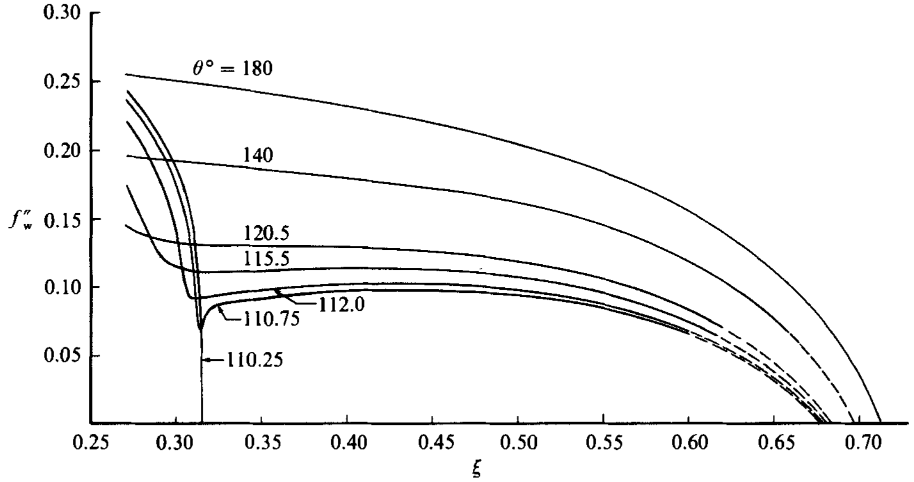

FIGURE 17. Variation of the streamwise wall shear f''_w with ξ in the second subregion. Dashed lines are assumed variations of f''_w.

corresponding to $\theta = 110.25$ to $\theta \geqslant 112$ and its variation is very smooth up to $\xi = 0.60$ and its value is finite. The behaviour of f''_w on the other $\theta =$ const. lines is also very smooth and finite up to $\xi = 0.60$. The skin-friction line with $\theta = 180$ also shows a similar behaviour. Again, except for $\xi = 0.7125$ where f''_w vanishes, the wall shear is always smooth and finite. We conclude from these results and from those of figure 16 that for $\xi \leqslant 0.60$, the magnitude of f''_w is finite and the solutions are essentially free of oscillations.

For $\xi > 0.60$, the stability parameter β begins to exceed 0.70 and, at subsequent values of ξ, the solutions begin to oscillate and do not allow the calculations to be performed for all values of θ up to 110.75°, as was the case for $\xi \leqslant 0.60$. The last θ-location becomes progressively worse as ξ increases. For example, the solutions for $\theta = 140°$ can be performed only up to $\xi = 0.67$ essentially without oscillations and for $\theta = 120.5°$, the last ξ-station free of oscillations is 0.6125.

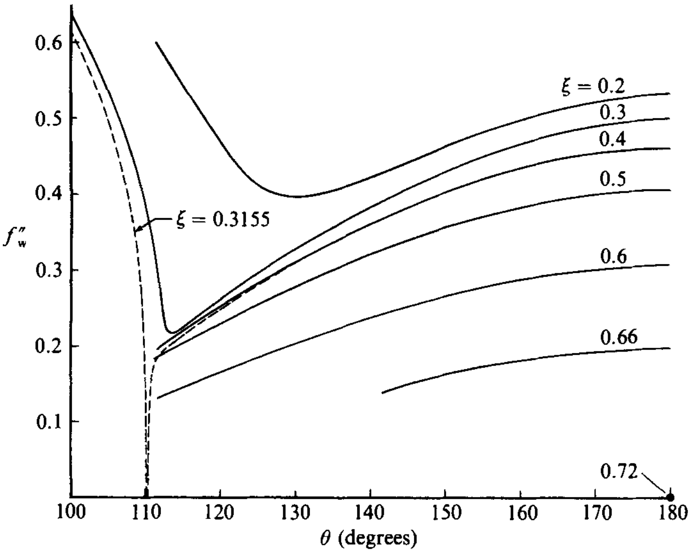

FIGURE 18. Variation of the streamwise wall shear f''_w with θ in the second subregion.

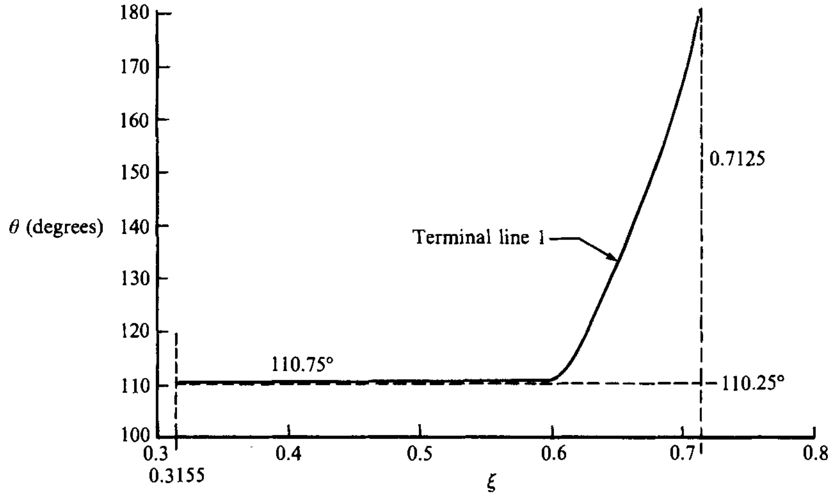

FIGURE 19. The boundaries of the second subregion.

Figure 19 shows a sketch of the second subregion and the variation of the 'terminal line 1' which represents the last θ-station where the solutions can be obtained without oscillations at a given ξ-location. As can be seen, for $\xi \leqslant 0.60$, the difference between the θ-line ($\equiv 110.25°$) that corresponds to $\xi_s = 0.3155$ and the terminal line 1 is only 0.50°, indicating that the nature of the 'upper separation' line of figure 2 is significantly different from the terminal line 1. We note from figure 20 that the behaviour of the limiting streamlines approaching the terminal line does not resemble that of those near an 'envelope' in that convergence of the streamlines is not apparent, and that the terminal line 1 does not correspond to a separation line. The direction of the limiting streamlines has been computed in terms of the angle they make with the ξ-axis, from

$$\gamma = \tan^{-1} \frac{g''_w}{f''_w}.$$

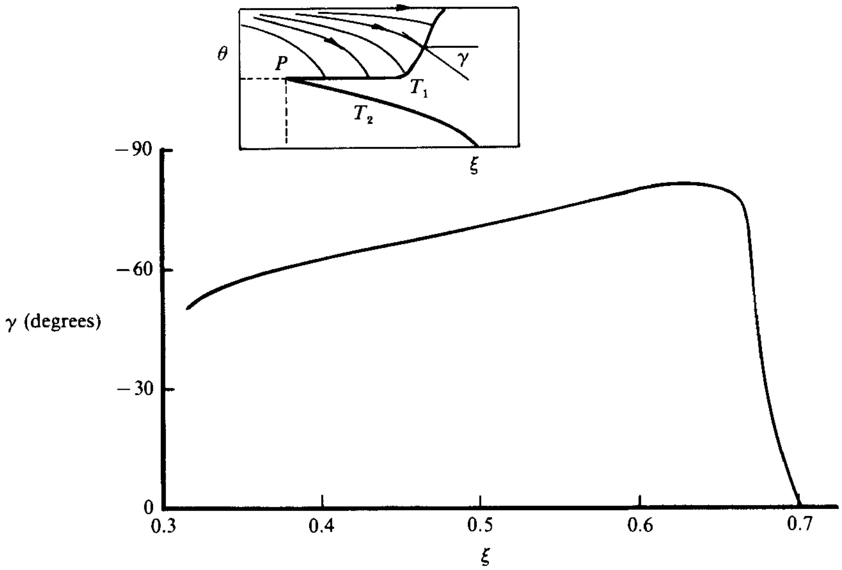

FIGURE 20. The variation of γ on the terminal line T_1. The insert shows the behaviour of the limiting streamlines.

θ (degrees)	r_k (degrees)
106–107.5	1.5
107.5–108.7	1.2
108.7–109.75	1.05

TABLE 8. θ-grid for the third subregion

This angle is zero on the leeward line of symmetry and varies along terminal line 1 from $-50°$ to $-80°$ for $0.3155 < \xi < 0.60$ and from $-80°$ to $0°$ as shown in figure 20. The increase in γ occurs rapidly over a very small range of θ near the line of 110.25°. We expect that if the calculations had extended beyond 110.75°, this angle would approach $-90°$, which represents the limit of the calculations since, for $\gamma < -90°$, information would be required from downstream.

5.3. *The third subregion*

This subregion, like that of §5.2, starts at $\xi_0 = 0.3155$ and extends to the windward separation point, $\xi_s = 0.8425$. It includes the domain between the windward line of symmetry and the separation line (see figure 2). Again we use a variable θ-grid similar to the one given in table 6 with a variable ξ-grid identical to that in table 7. For $0 \leqslant \theta \leqslant 106°$, the non-uniform θ-grid is the same as the one given in table 4 and for $106 \leqslant \theta \leqslant 109.75°$, it is given in table 8.

Calculations with the above grid, shown in figure 21, indicate that the stability parameter β is less than 0.2 everywhere. This is reflected in the results of figures 22 and 23 which show the variations of f''_w with ξ and θ for several values of θ and ξ, respectively. In contrast to the second subregion, the solutions are free of oscillations up to the θ-location where the streamwise wall shear f''_w vanishes. These results are in good agreement with those of Cebeci *et al.* (1981).

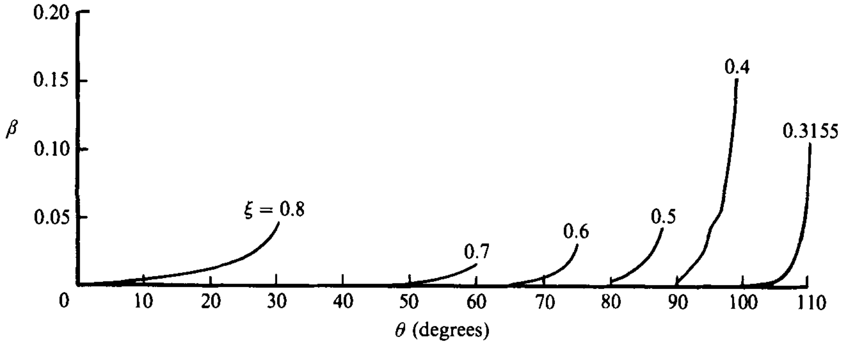

FIGURE 21. Variation of the stability parameter β with θ in the third subregion.

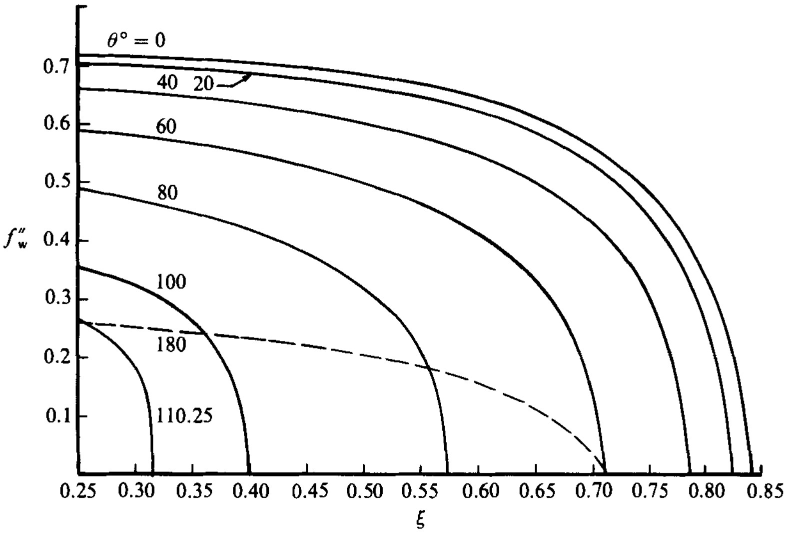

FIGURE 22. Variation of the wall shear f_w'' with ξ for constant values of θ in the third subregion. Dashed line denotes results for $\theta = 180°$.

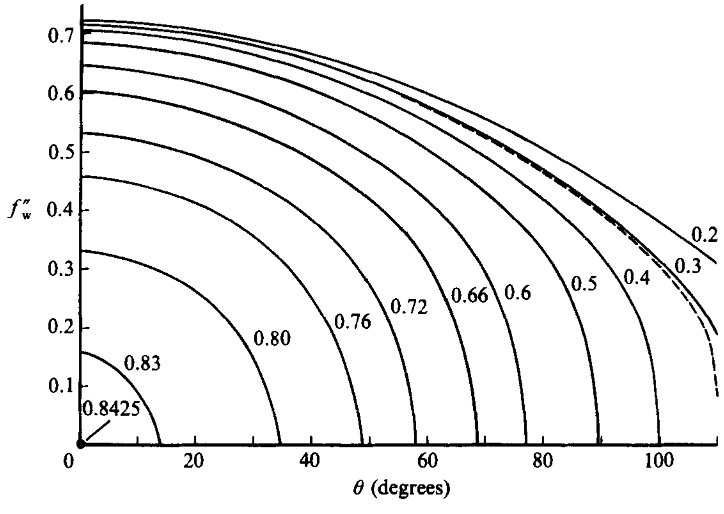

FIGURE 23. Variation of the wall shear f_w'' with θ for constant values of ξ in the third subregion. Dashed line denotes results for $\xi = 0.3155$.

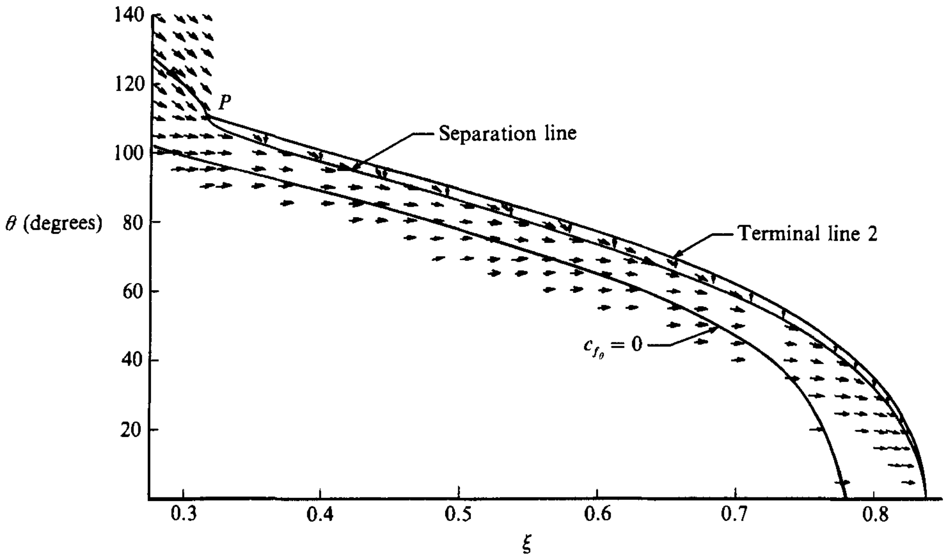

FIGURE 24. Terminal line 2, separation line and zero c_{f_θ}-line in the third subregion. The arrows denote the direction of the skin-friction line computed from g''_w/f''_w.

Figure 24 shows a sketch of the third subregion with three lines, corresponding to crossflow reversal, separation and terminal line 2 where f''_w is zero and $\gamma = -90°$. Cebeci *et al.* (1981) calculated similar crossflow reversal and terminal lines and deduced that separation would occur in close proximity to the latter. Present results confirm this deduction and show that the separation and terminal lines are a small distance apart. It is important to note that, in contrast to the earlier deduction, the present investigation does not support the view that three-dimensional separation corresponds to an envelope of limiting streamlines, and this topic is discussed further in the following section.

6. Nature of separation

There are several definitions of boundary-layer separation in three-dimensional flows, as discussed by Williams (1977). While they provide some insight into the nature of the separation phenomenon, they are of limited help in determining the nature of the flow in the vicinity of the separation line. The most useful interpretation of flow separation in three-dimensional flows is due to Lighthill (1963) and is based on the constant volume flow rate ϵ between two limiting streamlines separated by a distance h and two streamlines at a small distance y from the surface, i.e.

$$\epsilon = 0.5(\tau_x^2 + \tau_\theta^2)^{\frac{1}{2}} y^2 h. \tag{38}$$

Separation corresponds to the divergence of the streamlines from the surface, indicated by a drastic increase in y, and occurs if both τ_x and τ_θ approach zero or if h approaches zero. In the former case, the solutions are singular and a separation line begins at one singular point on the body. In the latter case, the resultant wall shear remains finite but the spacing between the limiting streamlines becomes very small. This type of separation in which the limiting streamlines coalesce with another limiting streamline is consistent with Lighthill's view that three-dimensional separation corresponds to a skin-friction line. It is not clear from (38), however, how

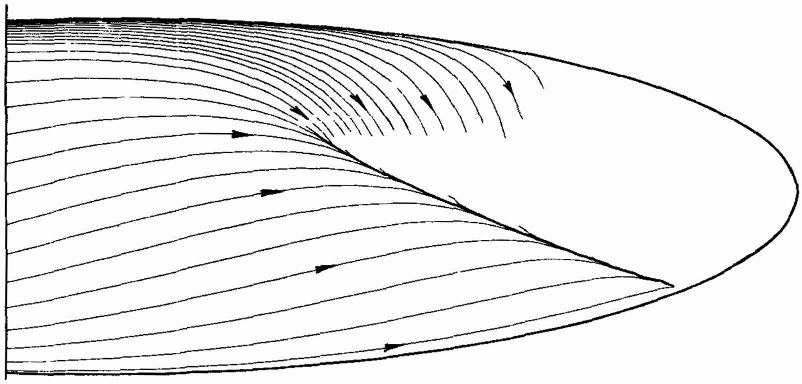

FIGURE 25. Behaviour of the limiting streamlines on the body.

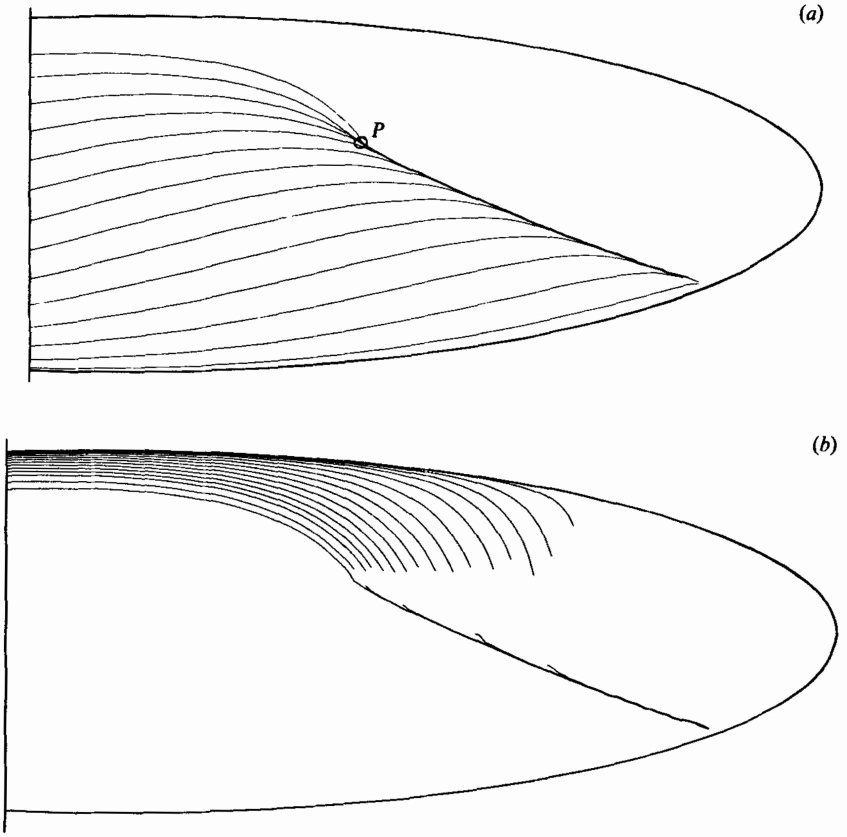

FIGURE 26. Behaviour of the limiting streamlines in the (*a*) third and (*b*) second subregions.

one can identify such a skin-friction line in a flow with open separation such as that considered here.

Figures 25 and 26 show the limiting streamlines obtained by integrating the direction field of the wall shear $h_1 g''_w/h_2 f''_w$ as a function of ξ and θ with integration starting at $\xi = -0.16$. We note that the streamlines are deflected from the ξ-direction owing to the effect of the stronger pressure gradient in the θ-direction. The flow is deflected initially in the θ-direction and turns back to the ξ-direction as the

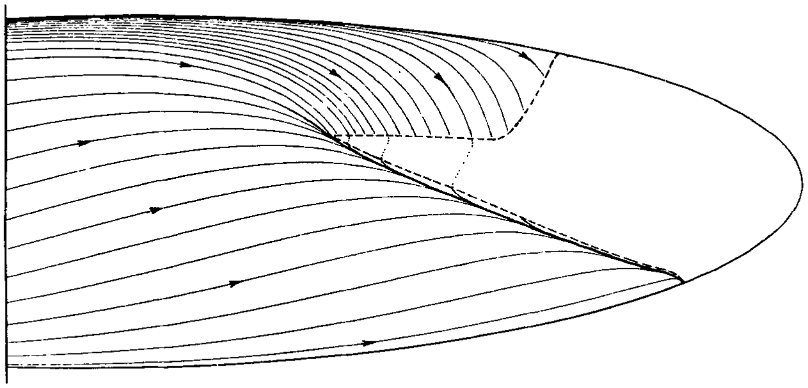

FIGURE 27. Conjectured behaviour of the limiting streamlines in the separated region between two terminal lines.

circumferential shear stress τ_θ becomes negative. With further increase in ξ, the streamwise pressure gradient becomes more adverse and causes a reduction in the streamwise wall shear f''_w. It appears from figure 25 that the first point that corresponds to negative g''_w and zero f''_w can be regarded as the beginning of the separation line and identifies the skin-fraction line as the separation line in three-dimensional flows: this point occurs at $\theta = 110.25°$ and $\xi = 0.3155$. The behaviour of the skin-friction lines on either side of the separation line is shown separately in figure 26. It is clear from figure 26(*a*) that the skin-friction line through the point P at $\theta = 110.25°$, $\xi = 0.3155$ has all the properties of the separation line proposed by Lighthill and that the other streamlines approach this line in a manner consistent with his arguments. Figure 26(*b*) shows a similar pattern of the limiting streamlines originating from terminal line 2. Although these streamlines are not as extensive as those from the windward line, owing to the small distance between the separation and the terminal lines, they have the same behaviour. It is also clear from figures 25 and 26(*b*) that there is no upper separation line as in figure 2.

The extension of calculations beyond terminal line 1 was discussed in §5.2, where it was pointed out that the angle between the skin-friction lines and the ξ-axis must exceed 90°. The principle be zones of dependence requires that information from higher values of ξ be provided and, since this information is not available, solutions of the boundary-layer equations cannot be obtained. Thus the flow between the two terminal lines cannot be determined by the present method. It may be conjectured, however, that the streamlines in Region C will follow the paths indicated by dotted lines on figure 27.

The blowing velocity v_w, that is,

$$v_w = \frac{1}{h_1 h_2}\left[\frac{\partial}{\partial x}(h_2 u_e \delta_x^*) + \frac{\partial}{\partial \theta}(h_1 w_e \delta_\theta^*)\right], \tag{39}$$

required to simulate the viscous/inviscid interaction provides another indication of flow separation together with the height of the displacement surface Δ which can be obtained by integrating the following expression along the inviscid streamlines ψ:

$$\frac{\mathrm{d}\Delta}{\mathrm{d}\psi} = \frac{1}{u_{se}}\left\{v_w - \Delta\left[\frac{\partial}{\partial x}(h_2 u_e) + \frac{\partial}{\partial \theta}(h_1 w_e)\right]\right\}, \tag{40}$$

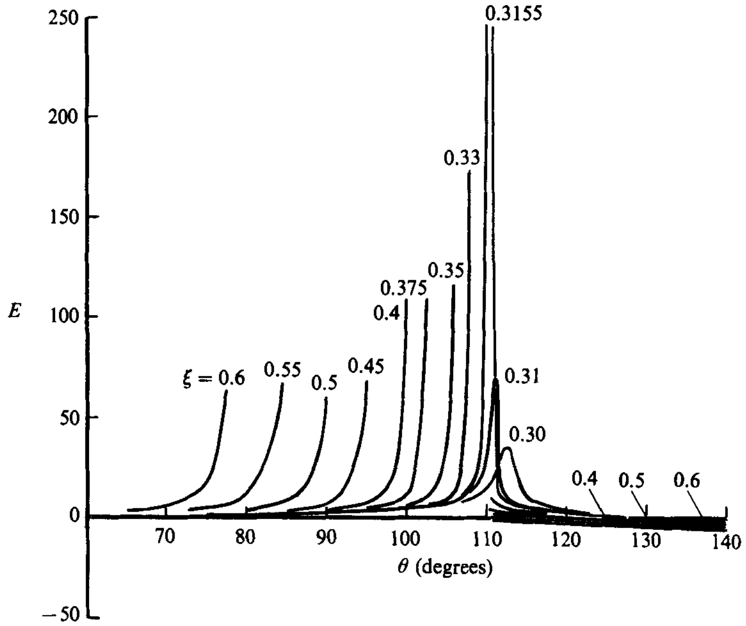

FIGURE 28. Variation of the dimensionless blowing velocity in the circumferential direction.

where u_{se} represents the resultant inviscid velocity. We note from (40) that large variation in v_w corresponds to large changes in the rate of growth of the displacement surface Δ and hence in the deflection of the streamlines away from the surface. Figure 28 shows the variation of the dimensionless blowing velocity E which is related to the dimensional blowing velocity v_w by

$$E = \frac{v_w}{u_e}(R_s)^{\frac{1}{2}} \tag{41}$$

where $R_s = u_0 s/\nu$. As in the previous calculations of Cebeci *et al.* (1981), the blowing velocity E is negative over a significant portion of the region of negative crossflow and the commonly held view that boundary layers under adverse pressure gradients act as blowing sources with respect to the external flow is seen not to be universally correct. The figure also shows that the blowing velocity E increases rapidly at the first separation point $\xi = 0.3155$ with similar behaviour on either side of this location and with very large magnitude. The blowing velocity has similar behaviour at other values of ξ as the solutions approach the conjectured separation line, and offers further support to the idea that the separation line in three-dimensional flows corresponds to a skin-friction line and to our procedure of identifying this line.

7. Concluding remarks

The following principal conclusions may be draw from the preceding text.

(i) The laminar flow pattern around the prolate spheroid at 6° angle of attack is complicated and includes a substantial region of circumferential flow reversal, a separation line and a region of open separation. Two terminal lines have also been determined and correspond to limits of applicability of the boundary-layer equations when solved with a prescribed external pressure distribution.

(ii) The numerical tests carried out in the region of positive crossflow velocity show that the accuracy of the characteristic box is similar to that of the regular box scheme provided that the stability criterion is maintained at a sufficiently small value.

(iii) In regions of substantial flow reversal in the circumferential direction, the choice of grid becomes increasingly important as the terminal and separation lines are approached. The stability criterion imposes a requirement for extremely small grid intervals so as to avoid numerical oscillations and to ensure accuracy. These observations are consistent with those previously made in relation to two-dimensional unsteady boundary-layer flows with substantial regions of flow reversal. The extension of the present procedure to include interaction with inviscid-flow equations or solutions of higher-order forms of the Navier–Stokes equations would encounter similar numerical constraints. This observation also applies to unsteady flows where earlier calculations with interaction showed the need to satisfy the stability criterion with consequent small grid intervals in space and time.

(iv) The results reveal a single separation line in contrast to earlier calculations performed without consideration of numerical accuracy. The nature of this separation line supports Lighthill's view that separation in three-dimensional boundary-layer flows is a skin-friction line rather than the envelope of limiting streamlines suggested by others.

(v) A procedure is proposed to identify the separation line which involves the determination of the skin-friction line that passes through the first location at which the longitudinal shear stress is zero and the circumferential shear stress is negative.

This work was sponsored by the Air Force Office of Scientific Research under contract F49620-84-C-0007.

REFERENCES

Bradshaw, P., Cebeci, T. & Whitelaw, J. H. 1981 *Engineering Calculation Methods for Turbulent Flow*. Academic.

Cebeci, T. (ed) 1986*a* *Numerical and Physical Aspects of Aerodynamic Flows III*, Part 4, pp. 341–464. Springer.

Cebeci, T. 1986*b* Unsteady boundary layer with an intelligent numerical scheme. *J. Fluid Mech.* **163**, 129–140.

Cebeci, T. 1986*c* An approach to practical aerodynamic calculations. *VKI Lecture Series on Computation of Three-Dimensional Boundary Layers.*

Cebeci, T. & Bradshaw, P. 1984 *Physical and Computational Aspects of Convective Heat Transfer.* Springer.

Cebeci, T., Kaups, K. & Khattab, A. A. 1986 Separation and reattachment near the leading edge of a thin wing. *IUTAM Proc.* Springer.

Cebeci, T., Khattab, A. A. & Schimke, S. M. 1987 Separation and reattachment near the leading edge of a thin oscillating airfoil. *Douglas Rept. MDC* J4847.

Cebeci, T., Khattab, A. A. & Stewartson, K. 1980 On nose separation. *J. Fluid Mech.* **97**, 435–454.

Cebeci, T., Khattab, A. A. & Stewartson, K. 1981 Three-dimensional laminar boundary layer and the ok of accessibility. *J. Fluid Mech.* **107**, 57–87.

Crank, J. & Nicholson, P. 1947 A practical method for numerical evaluation of solutions of partial differential equations of the heat-conduction type. *Proc. Camb. Phil. Soc.* **43**, 50–67.

Keller, H. B. 1974 Accurate difference methods for two-point boundary-value problems. *SIAM J. Num. Anal.* **11**, 305–320.

Lighthill, M. J. 1963 In *Laminar Boundary Layers* (ed. L. Rosenhead), Cha. 2, p. 79. Oxford University Press.

MASKELL, E. C. 1955 Flow separation in three dimensions. *Aero. Res. Coun.* 18063.

RAETZ, G. S. 1957 A method of calculating three-dimensional laminar boundary layers of compressible flows. *Northrop Corp. Rep. NAI* 58–73.

WANG, K. C. 1975 Boundary layer over a blunt body at low incidence with circumferential reverse flow. *J. Fluid Mech.* **72**, 49–65.

WILLIAMS, J. C. 1977 Incompressible boundary-layer separation. *Ann. Rev. Fluid Mech.* **9**, 113–144.